Paper No.
18793

AMPP ANNUAL CONFERENCE + EXPO
MARCH 19-23, 2023 | DENVER, COLORADO

Developing an Appropriate Heat Treatment Protocol for Additively Manufactured Alloy 718 for Oil and Gas Applications

M.R. Stoudt
Material Measurement Laboratory
National Institute of Standards and Technology
Gaithersburg, MD, USA 20899

M.E. Williams
Material Measurement Laboratory
National Institute of Standards and Technology
Gaithersburg, MD, USA 20899

J.S. Zuback,
Material Measurement Laboratory
National Institute of Standards and Technology
Gaithersburg, MD, USA 20899

K.W. Moon
Material Measurement Laboratory
National Institute of Standards and Technology
Gaithersburg, MD, USA 20899

C.E. Campbell
Material Measurement Laboratory
National Institute of Standards and Technology
Gaithersburg, MD, USA 20899

C.R. Beauchamp
Material Measurement Laboratory
National Institute of Standards and Technology
Gaithersburg, MD, USA 20899

M. Yunovich
Shell Technology Center Houston
3333 Highway 6 South
Houston, TX 77082

ABSTRACT

The combination of strength, corrosion resistance, and excellent weldability makes Alloy 718 an attractive alloy for additive manufacturing (AM) applications, but the AM build process generates large compositional and microstructural heterogeneities. The formation of the δ-phase is of particular importance within the petroleum and natural gas (PNG) industries and a reduced Nb content is one method currently in use to control δ-phase growth in wrought IN718. However, it is not clear how effective that strategy will be in AM components as the growth kinetics of δ -phase are exceptionally sensitive to the build parameters used in the AM processing. Since the API 6ACRA treatment protocol used for wrought Alloy 718 does not produce the same properties in AM 718, a refined post-build heat treatment is required to relieve residual stresses and produce uniform microstructures and properties. An integrated computational materials engineering (ICME) framework was adopted for this work to develop an effective heat treatment protocol for AM-processed IN718 that consistently achieves the requisite performance metrics while minimizing the δ-phase growth. for oil and gas industry applications. The results revealed that even though the wrought heat treatment does not completely remove all the AM solidification microstructure, it was sufficient to precipitate γ' to achieve the 1035 MPa (150 ksi) strength level. Precipitation of γ", which governs the 850 MPa (120 ksi) strength level, is far more difficult to achieve without significant co-precipitation of the δ-phase. Additional characterizations and model

© 2023 Association for Materials Protection and Performance (AMPP). All rights reserved. No part of this publication may be reproduced, stored in a retrieval system, or transmitted, in any form or by any means (electronic, mechanical, photocopying, recording, or otherwise) without the prior written permission of AMPP.
Positions and opinions advanced in this work are those of the author(s) and not necessarily those of AMPP. Responsibility for the content of the work lies solely with the author(s).

refinements are in progress to optimize the γ' and γ'' precipitation and to control the precipitation of the δ-phase.

Key words: Additive manufacturing, PBF, Alloy 718, API 6ACRA, heat treatment, δ-phase

INTRODUCTION

Additive manufacturing (AM) is a transformative technology that has opened areas of design space that were previously inaccessible by enabling the production of complex, three-dimensional parts and intricate geometries that were impractical to produce via traditional manufacturing methods [1, 2]. However, the extreme thermo-mechanical conditions in the AM build process (e.g., cooling rates ranging from 103 K/s to 106 K/s and repeated heating/cooling cycles) generate deleterious microstructures with high residual stresses, and extreme compositional gradients. As such, AM-processed components typically exhibit regions with substantially different local chemistries, microstructures, and undesirable phases [3, 4]. Most of the current heat treatment protocols were designed to be used with wrought materials with nominal compositions and equilibrium phase diagrams. When applied to AM-processed components, these protocols can generate microstructures that severely degrade the mechanical performance of the AM-processed part [5-7]. For this reason, the relationships between the AM processing conditions and post-build heat treatments and the properties and performance of industrially important alloys needs to be evaluated. The environmentally assisted cracking resistance is one such property.

Inconel 718 (IN718, Alloy 718) is a well characterized precipitation-strengthened nickel-based superalloy that is currently being evaluated for applications within the oil and gas industry largely due to the wide range of desirable properties (e.g., weldability, creep resistance and corrosion resistance). However, AM-processing generates many of the same complications observed in AM-processed IN625 [3, 5, 8, 9]. That is, the pronounced segregation of solute elements that occurs during solidification significantly increases the likelihood of the precipitation of various secondary intermetallic phases such as Laves phases, topologically close-packed (TCP) phases, carbides, and δ-phase ($D0_a$ Ni_3Nb) that can deleteriously influence the properties during service [10-14]. The formation of the δ-phase is of particular importance within the petroleum and natural gas (PNG) industries. Previous research on AM-processed Ni-based superalloys revealed that δ-phase forms as fine platelets within the Nb-rich interdendritic regions in the as-deposited solidification microstructure [5, 6, 8]. Depending on the conditions in the service environment, the growth kinetics of δ-phase can be rather slow in a homogenized microstructure (i.e., hundreds of hours), but when the platelets do reach critical size, they degrade the fracture toughness considerably [15, 16, 17]. The growth kinetics for δ-phase are exceptionally sensitive to temperature, alloy composition, and the build parameters used in the AM processing [18-20].

A recent study [21] showed that when δ-phase and hydrogen are present in the matrix of an AM-processed IN625, it substantially reduces both the ductility and the crack propagation resistance. Considering that the concentration of Nb in IN625 is similar to IN718, one can expect a similar effect in IN718. In addition, δ-phase can exacerbate local embrittlement by promoting hydrogen trapping along the δ-phase/matrix interface [22]. Thus, control of the growth of δ-phase is critical since this could have potentially catastrophic implications regarding the use of AM-processed components in a hydrogen-rich service environment. One method currently in use by the PNG industry to control δ-phase growth in wrought IN718 is specifying a lower Nb content. However, it is not clear if that strategy will be as effective in AM components.

This study presents from an examination of the performance of nickel-based superalloys under environmental conditions that simulate those in service in the PNG industry. The primary goal of this facet of the study was to develop an effective heat treatment protocol for AM-processed IN718 that consistently achieves the requisite performance metrics for oil and gas industry applications while minimizing the δ-phase growth.

© 2023 Association for Materials Protection and Performance (AMPP). All rights reserved. No part of this publication may be reproduced, stored in a retrieval system, or transmitted, in any form or by any means (electronic, mechanical, photocopying, recording, or otherwise) without the prior written permission of AMPP.
Positions and opinions advanced in this work are those of the author(s) and not necessarily those of AMPP. Responsibility for the content of the work lies solely with the author(s).

An integrated computational materials engineering (ICME) framework and a systems approach were adopted to achieve this objective [23]. A system chart is a convenient construction depicting the relationships between the four primary elements in materials science and engineering: processing, structure, properties, and performance [24]. Figure 1 shows the processing-structure-property (PSP) relationships for a PNG-grade IN718. The column on the left highlights the AM-specific processing conditions used. The structure column in the middle emphasizes the microstructure elements that dominate the material behavior. The properties listed in the right column are the key materials properties defining the needed performance for an oil-gas application. The lines between the processing and structure elements indicate the processing steps that dominate each microstructure element. Similarly, the lines between the structure and properties represent the microstructural features that dominate a particular material property. Understanding these processing-structure-property relationships provides insight into what critical relationships are needed to control and optimize the performance of the material. Analysis of the PSP relationships also reveals the trade-offs that may be necessary to accommodate conflicting property objectives. For this application, the environment cracking resistance was identified as the ultimate performance criterion for this alloy, and that is dependent on the following mechanical properties: tensile strength, impact resistance, fracture toughness, and fatigue resistance. These properties can all be optimized by reducing or eliminating the δ-phase precipitation, optimizing the γ' and γ'' precipitation, and optimizing the grain size. As shown in the figure, the AM processing controls the initial solidification structure, which determines the amount of micro-segregation. That is, higher amounts of micro-segregation present in the solidification microstructure will require a higher temperature and/or a longer homogenization time, which will increase the final grain size. Accordingly, if the initial micro-segregation cannot be minimized during the build process, a trade-off must be made between a tolerable residual micro-segregation or a larger grain size in the material. Similarly, the solutionizing and aging heat treatments determine the amount γ' and γ'' precipitation and how much δ-phase may be present. An additional compromise may be required between avoiding the formation of δ phase and maximizing the precipitation of γ' and γ'' phases. The initial powder composition and atomization processing will determine the presence of secondary phases such as carbides and intermetallic phases.

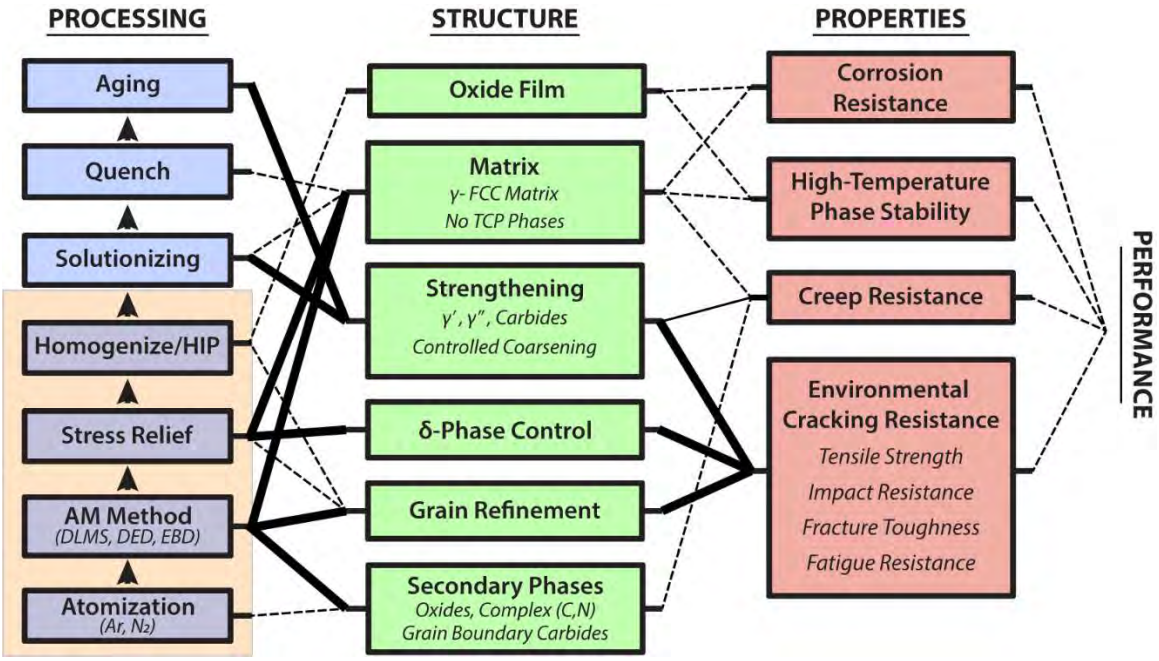

Figure 1: A system chart showing the relationships between processing, microstructure and properties in a Ni-based superalloy. The chart is focused on the factors that influence the performance of a PNG-grade IN718 alloy in an oil and gas application. The bold lines between individual boxes indicates a strong dependence.

© 2023 Association for Materials Protection and Performance (AMPP). All rights reserved. No part of this publication may be reproduced, stored in a retrieval system, or transmitted, in any form or by any means (electronic, mechanical, photocopying, recording, or otherwise) without the prior written permission of AMPP.
Positions and opinions advanced in this work are those of the author(s) and not necessarily those of AMPP. Responsibility for the content of the work lies solely with the author(s).

The American Petroleum Institute (API) 6ACRA Standard [25] identifies two strength levels / conditions for IN718 in oil and gas applications: 825 MPa (120 ksi) and 1035 MPa (150 ksi). The higher strength level is achieved through a two-step precipitation heat treatment, and considering that each step precipitates a different phase, it was determined to be the more complex of the two heat treatments. As such, the ICME / system approach was used to optimize the properties to achieve the higher strength level in this research.

EXPERIMENTAL PROCEDURE

Additively processed specimens were built at the Shell Amsterdam 3DP center from virgin IN718 powder with a laser powder bed fusion (LPBF) system and a standard parameter set. The powder conformed to the composition guidelines recommended by the 6ACRA standard for the N07718 alloy shown in Table 1 [25]. Using the orientation nomenclature in ISO/ASTM 52900-15 [26], specimens for this analysis were built with the '*z*' direction (i.e., the build direction) perpendicular to the *x*-*y* plane (i.e., the build plate). One set of specimens was built with a 12mm cross section to create a solidification microstructure that would be representative of the cooling rate in a thin cross section. Similarly, an 80 mm cube was built to create a solidification microstructure that would be representative of the cooling rate in a thicker cross section. Upon completion, the build was solutionized / annealed for 2h at 1050°C and air cooled to room temperature following the heat treatment protocol recommended by the 6ACRA standard (1h to 2.5h at 1021°C to 1050°C). The specimens were then cut from the plate using wire electro-discharge machining (EDM) and prepared for analysis. Hereafter, these samples were designated as the 'SA' condition. In addition, a set of samples that received no additional thermal processing (hereafter designated as the 'as-deposited' or 'AD' condition) and a set cut from a wrought bar (designated as 'W') of similar composition were also included in this evaluation to provide a basis for comparison.

Specimens in the SA condition with both thick and thin cross sections were encapsulated in quartz tubes for heat treatment that was designed reproduce the 1035MPa (150 ksi) strength level described in the 6ACRA standard [25]. This two-step precipitation heat treatment protocol consisted of an isothermal hold for a minimum of 8h at a temperature between 700°C and 750 C (725°C was selected), followed by a furnace cool to a temperature between 600°C and 650°C and a second isothermal hold for a minimum of 8h (625°C was selected). Samples that were given this heat treatment were given an additional designation of 6ACRA. An additional set of samples were given an additional heat treatment to ensure complete homogenization of the composition and to eradicate any remnants of the solidification microstructure. This heat treatment, based on the results shown by Zhao et al. [13], was 0.5h at 1175°C. Samples with this heat treatment were designated as the SA+H condition.

Laboratory-based X-ray diffraction (XRD) measurements were performed using Cu *Kα* radiation and a 2D area detector to determine the phases present in the AD, SA, and W samples and were consistent with those described in references [5] and [7]. Partial diffraction rings were acquired in the 2θ range of 30° to 60° using a step size of 0.02° and 5s counting time per step. The intensity at each 2θ step was integrated along the partial diffraction ring to generate intensity vs. 2θ plots. The peaks were indexed using powder diffraction files from the Inorganic Crystal Structure Database at the National Institute of Standards and Technology [27].

Samples in the W, SA, (SA+6ACRA), and the (SA+H+6ACRA) conditions were prepared for hardness testing. A set of AM samples was cut from the 80 mm cube with EDM and had a nominal geometry of 13x13x80 mm. A 12mm thick sample was also cut with EDM from the 50mm diameter wrought bar. Two parallel surfaces (i.e., top and bottom) were ground to a coplanar 1µm diamond finish on each hardness specimen using standard metallographic procedure [28]. The top surfaces were then indented using a procedure consistent with the ASTM Standard E18 for Rockwell hardness testing [29]. A minimum of 30 indentations were made on each specimen with a spacing between the individual impressions sufficiently large to prevent overlap between the plastic strain fields.

© 2023 Association for Materials Protection and Performance (AMPP). All rights reserved. No part of this publication may be reproduced, stored in a retrieval system, or transmitted, in any form or by any means (electronic, mechanical, photocopying, recording, or otherwise) without the prior written permission of AMPP.
Positions and opinions advanced in this work are those of the author(s) and not necessarily those of AMPP. Responsibility for the content of the work lies solely with the author(s).

RESULTS

The alloy composition shown in Table 1 was used to predict both the phases likely to form during solidification and the composition and amount of the stable phases after appropriate heat treatment. These predictions were made using the Thermo-Calc[1] (TC)-2022b software suite [30], the TC-Ni11 thermodynamic database [31], and the TC-MobNi5 mobility database [32].

Table 1. IN718 Alloy N07718 Composition

Element	6ACRA Allowable Composition,%	Measured Composition, %
Ni	50.0 to 55.0	53.3
Cr	17.0 to 21.0	18.6
(Nb + Ta)	4.87 to 5.20	5.17
Fe	Balance	18.33
Mo	2.80 to 3.30	2.91
Al	0.40 to 0.60	0.55
Ti	0.80 to 1.15	0.91
Cu	0.23 max	0.03
Co	1.00 max	0.04
B	0.0060 max	0.001
C	0.045 max	0.03
Mn	0.35 max	0.05
P	0.010 max	0.001
S	0.010 max	0.001
Si	0.35 max	0.05
N	---	0.007
O	---	0.0176

Figure 2 is a Scheil-Gulliver simulation illustrating the non-equilibrium solidification behavior for this composition. An analysis of this type provides a wide range of information regarding the solidification. For example, it reveals the temperature range over which solidification is expected to occur for a given composition. It also reveals the depression of the solidus temperature produced by the segregation, the composition of the last liquid to solidify in the interdendritic regions, and the phases formed in the segregated regions of the solid. Additionally, a Scheil simulation predicts the segregation profile and composition gradients in the primary (or matrix) phase, which enables the design of appropriate heat treatment protocols to eradicate the segregation and homogenize the composition. Classically, a Scheil model assumes that there is no diffusion in the solid phases once they have formed, that there is infinitely fast diffusion in the liquid at all temperatures, and that equilibrium exists at the solid liquid interface [33, 34]. The initial cooling rates in LPBF are on the order of 10^6 K/s, which are substantially faster than those in a typical casting. However, the as-deposited material will often re-solidify when a new layer of powder is deposited [6, 35]. This solidification process may much slower than the initial rapid solidification that occurs during the deposition. As such, the simulation had to be adjusted to account for the higher solidification rates [36]. This was accomplished by assuming that both the carbon and nitrogen in the composition were fast diffusing elements. Both are interstitial elements and are known to diffuse freely

[1] Thermo-Calc, Thermo-Calc Software AB, Stockholm, Sweden, 2022. All rights reserved.
Certain commercial entities, equipment, or materials may be identified in this document to describe an experimental procedure or concept adequately. Such identification is not intended to imply recommendation or endorsement by the National Institute of Standards and Technology, nor is it intended to imply that the entities, materials, or equipment are necessarily the best available for the purpose.

© 2023 Association for Materials Protection and Performance (AMPP). All rights reserved. No part of this publication may be reproduced, stored in a retrieval system, or transmitted, in any form or by any means (electronic, mechanical, photocopying, recording, or otherwise) without the prior written permission of AMPP.
Positions and opinions advanced in this work are those of the author(s) and not necessarily those of AMPP. Responsibility for the content of the work lies solely with the author(s).

throughout the solid. The simulation still assumed that the diffusion in the liquid phase was infinitely fast, but this modification also allowed for limited diffusion in the primary phase of the solid material, and it accounted for any back diffusion that may have occurred in the primary solid phase. Additionally, including fast diffusing elements in the simulation also allowed for infinite diffusivity of those elements to occur in the solid phases [30].

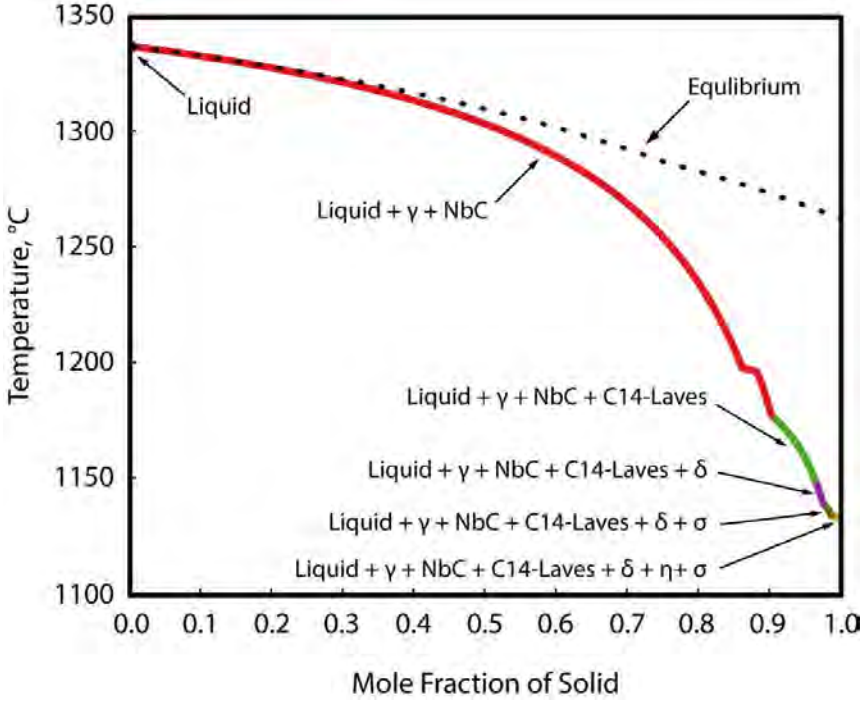

Figure 2: Scheil-Gulliver simulation illustrating the non-equilibrium solidification behavior in a PNG-grade IN718 alloy.

The dotted line in Figure 2 represents the solidification behavior under equilibrium conditions, and the solid line shows both the depression that occurs in the solidus temperature during the solidification of the N07718 alloy and the phases that could form. In addition to the matrix phase (g), the simulation predicts the formation of several phases near the terminal stages of solidification, such as d, s, and h, but these phases were not observed in the subsequent analyses. It is well-known that the assumptions of calculations under Scheil assumptions break down near the end of solidification and deviate from experimental observations. However, the simulation predicts the formation of the C14 Laves phase and the Nb-rich MC carbide, which were observed in the microstructure. Laves phases are brittle intermetallic phases that are known to adversely affect mechanical properties when present. In nickel-based superalloys, Laves phase are known to deplete Nb in the matrix thereby significantly reducing the phase fractions of the strengthening precipitates (i.e., γ' and γ'') [37].

As shown in Figure 3, XRD confirmed the presence of the MC carbide and Laves phase in the AD condition. However, the XRD results also revealed that Laves phase was not present after the application of a suitable solutionization heat treatment, and that the MC carbide was only the significant phase present. In this alloy, the MC carbide is typically NbC, but as shown in Table 1, this composition also contains 0.007% nitrogen, which could promote the formation of the Nb(C,N) carbo-nitride. Since both phases are Nb-rich, they could also locally deplete the Nb in the matrix phase if they are allowed to grow.

© 2023 Association for Materials Protection and Performance (AMPP). All rights reserved. No part of this publication may be reproduced, stored in a retrieval system, or transmitted, in any form or by any means (electronic, mechanical, photocopying, recording, or otherwise) without the prior written permission of AMPP.
Positions and opinions advanced in this work are those of the author(s) and not necessarily those of AMPP. Responsibility for the content of the work lies solely with the author(s).

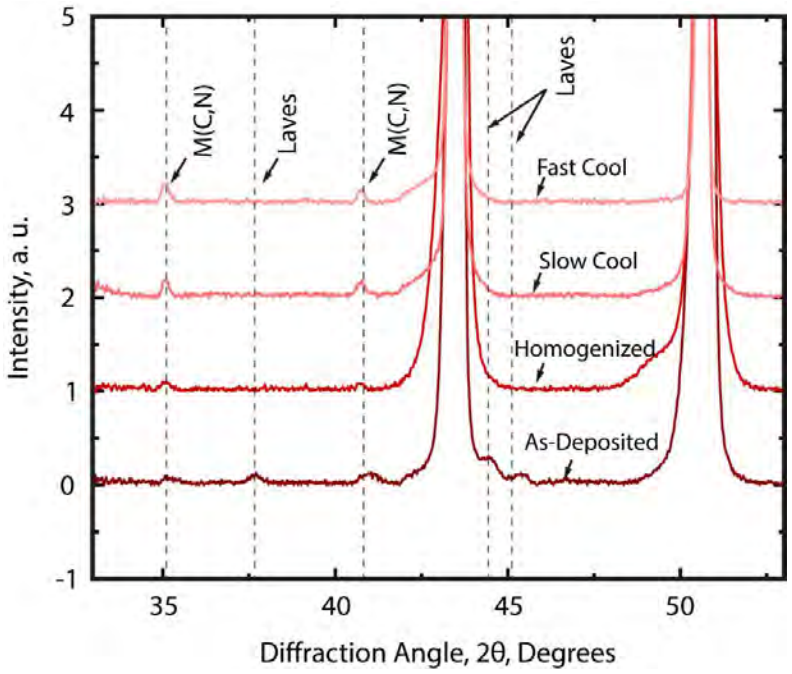

Figure 3: XRD patterns for the IN718 alloy in the as deposited, the solutionized condition under fast and slow cooling rate conditions, and after homogenization.

The results of microstructural characterizations performed on the four conditions in Figure 3 are shown in Figure 4. All the surfaces shown in the figure are in the XY orientation and were electrolytically etched with a 10% (volume fraction) chromic acid solution. The AD condition (Figure 4a) shows the typical cellular / dendritic structure that is consistent with a solidification microstructure. Electron energy dispersive spectroscopy (EDS) analyses revealed that the dendrite cores (the darker regions in the figure) were slightly enriched in both Ni and Cr and that the interdendritic regions (the bright regions) were enriched in Nb, Ti, and Mo. After solutionizing for 2h at 1050°C, the composition was homogenized, at least to the level of detection with EDS, and exhibited a twinned microstructure that was consistent with that of a Ni-based alloy. However, additional examination revealed the presence of several remnants of the solidification microstructure. These remnants were observed in the SA condition with both the fast cool (Figure 4b), and the slow cool (Figure 4c). Some differences were also observed in the concomitant microstructures. As shown in Figure 4b and Figure 4c, the cooling rate appeared to affect the character of the cellular structure to some degree, but the presence of the large Nb-rich carbides along the interface in the slow cooled material was the more noticeable difference. While the additional homogenization heat treatment eliminated all remnants of the solidification microstructure (Figure 4d), the additional 0.5h at 1175°C also promoted rampant grain growth, and as a result, the microstructure shown in Figure 4d only encompassed one grain. In addition, the exceptionally large grain size substantially reduced the efficacy of the etch, which in turn, affected the image contrast. (Note that the scale bar in Figure 4d is an order of magnitude larger than those in the other images in the figure.)

© 2023 Association for Materials Protection and Performance (AMPP). All rights reserved. No part of this publication may be reproduced, stored in a retrieval system, or transmitted, in any form or by any means (electronic, mechanical, photocopying, recording, or otherwise) without the prior written permission of AMPP.
Positions and opinions advanced in this work are those of the author(s) and not necessarily those of AMPP. Responsibility for the content of the work lies solely with the author(s).

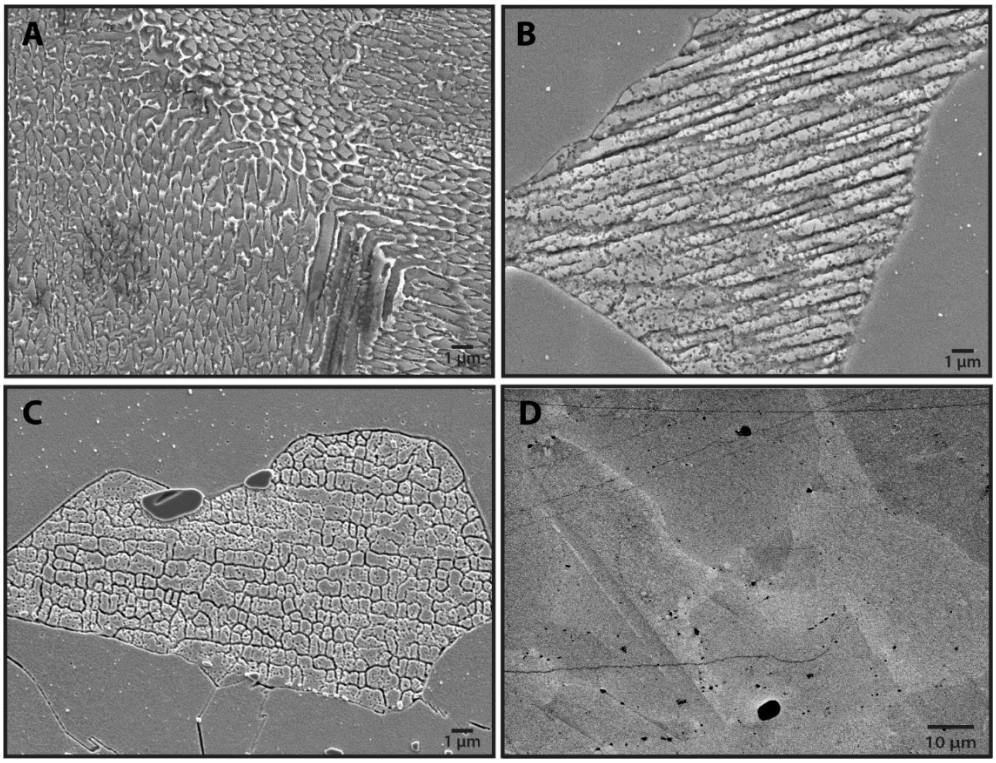

Figure 4: Scanning electron micrographs showing the structure of the four conditions shown in Figure 3. a) As deposited with no additional thermal processing, b) Solutionized for 2h at 1050°C under fast cooling rate conditions, c) Stress relieved/solutionized for 2h at 1050°C under slow cooling rate conditions, and d) Homogenized for 0.5h at 1175°C. Note the scale bar in Figure 4d is an order of magnitude larger than those in the other images in this figure.)

The predicted equilibrium phase fractions for this composition are shown in Figure 5. The temperature range in the figure was compressed to isolate the phases in the alloy that are of greatest importance to the PNG industry. Assuming a chemically homogenous composition (i.e., no micro-segregation) over the temperature range, the figure shows the fractions of the thermodynamically stable phases. As expected, the matrix phase (g) is the dominant phase over the entire temperature range, but the phase fraction of δ-phase is also predicted to be significant at temperatures below 1000°C. The figure also indicates that the MC carbide is stable above 650°C, and that the γ' phase is stable below 925°C. The γ'' phase is noticeably absent in Figure 5, and the reason it does not appear is that γ'' is not an equilibrium phase in this alloy. The simulation shown in Figure 5 was then recomputed under constrained equilibrium conditions that suspended the formation of the δ-phase and the results from that simulation are shown in Figure 6. When the δ-phase is not allowed to form under the constrained equilibrium conditions, the simulation revealed that γ'' does indeed form, and that the phase fraction is similar to that of the δ-phase below 925°C. This is an indication of the importance of precipitation kinetics in defining the material properties for this alloy.

© 2023 Association for Materials Protection and Performance (AMPP). All rights reserved. No part of this publication may be reproduced, stored in a retrieval system, or transmitted, in any form or by any means (electronic, mechanical, photocopying, recording, or otherwise) without the prior written permission of AMPP.
Positions and opinions advanced in this work are those of the author(s) and not necessarily those of AMPP. Responsibility for the content of the work lies solely with the author(s).

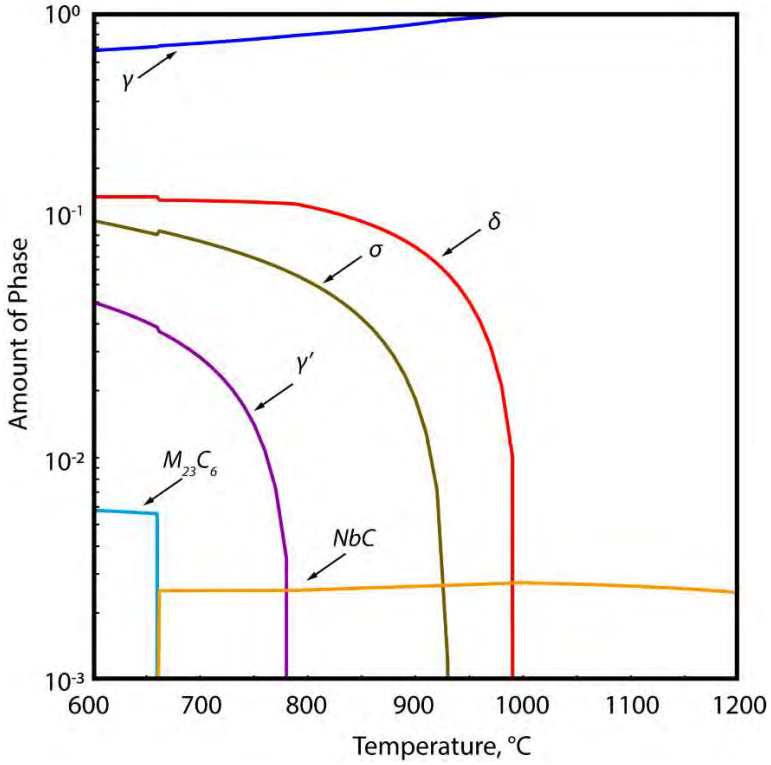

Figure 5: The predicted equilibrium phase fractions for the composition shown in Table 1 after homogenization. Note that the g'' strengthening precipitate phase is not shown in this figure because it is not an equilibrium phase.

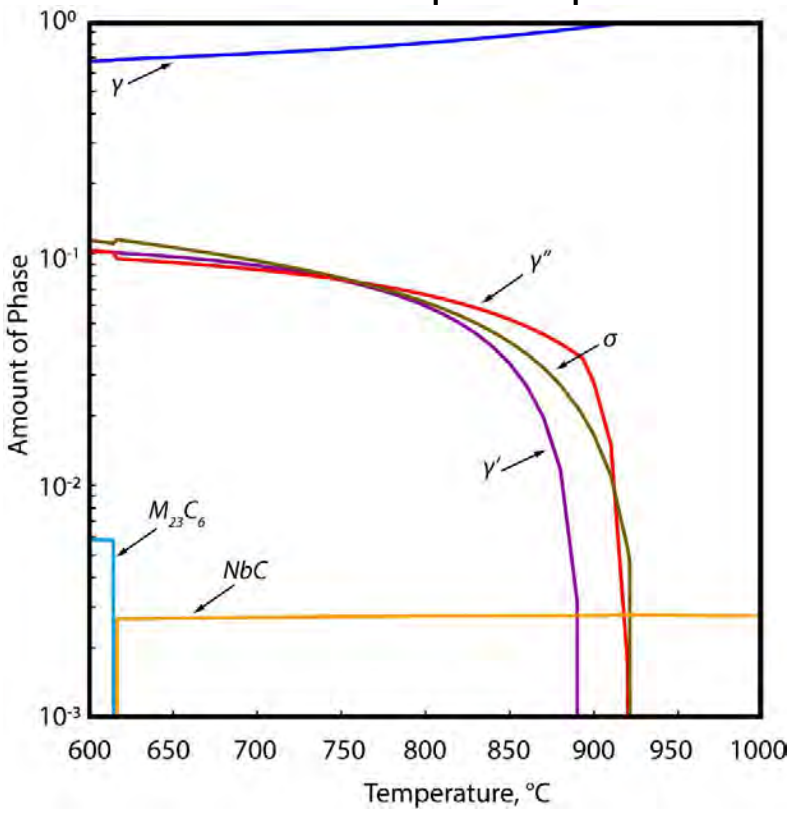

Figure 6: The predicted phase fractions under constrained equilibrium conditions for the composition shown in Table 1 after homogenization.

© 2023 Association for Materials Protection and Performance (AMPP). All rights reserved. No part of this publication may be reproduced, stored in a retrieval system, or transmitted, in any form or by any means (electronic, mechanical, photocopying, recording, or otherwise) without the prior written permission of AMPP.
Positions and opinions advanced in this work are those of the author(s) and not necessarily those of AMPP. Responsibility for the content of the work lies solely with the author(s).

Figure 6 also shows that the phase fractions and the stable temperature ranges of the other predicted phases increased significantly. For example, under normal equilibrium conditions, γ' was stable below 725°C with a maximum phase fraction of approximately $3.5x10^{-2}$, whereas under constrained equilibrium conditions, γ' is stable below 875°C with a predicted maximum phase fraction of approximately 10^{-1}. Note that these plots reflect the fractions of the phases that are possible for these compositions at equilibrium and do not consider the rate at which any of those phases may form. As such, these figures are approximations; yet they do illustrate the influence a small change in the Nb content can produce in this alloy.

Both Figure 5 and Figure 6 indicate a significant phase fraction of σ-phase. The literature indicates that σ-phase is a topologically closed packed (TCP) phase that forms in many Ni-based superalloys [38]. Although the actual composition of σ-phase depends on the alloy composition, it characteristically is rich in Ni, Cr and Mo. Considering that TCP precipitates are usually brittle and tend to nucleate along grain boundaries, they are considered detrimental because they reduce grain boundary cohesion and promote crack propagation. However, the formation kinetics for σ-phase are substantially slower compared to the rate at which δ-phase forms in this alloy, and for this reason, it is assumed σ-phase will not be present in any significant quantity for a substantially long time under normal service conditions.

As noted earlier, one of the objectives of this research was to develop a heat treatment protocol that would consistently meet the performance specifications for the 6ACRA-150 strength level. One of the more straightforward ways to evaluate strength is to compare the relative hardness values for different conditions. Considering that it is used extensively throughout industry, the Rockwell Hardness-C scale (hereafter designated as HRC) was the most appropriate method to assess the hardness and was adopted for this work. According to the 6ACRA Standard, the HRC values for the N07718 alloy in the 6ACRA-150 condition should be no less than 35HRC, and the maximum should not exceed 45HRC.

The relevant statistical parameters derived from the individual HRC test data are presented as a simple box and whisker plot in Figure 7. A box plot is a convenient method to graphically represent the minimum, the maximum, the median, and the first and third quartiles in a given dataset [39, 40]. Considering that the features in a box and whisker plot can represent several different statistical parameters, the boxes in this figure reflect the following: The boxes were drawn from the first quartile (i.e., the median of the lower half of the dataset) to the third quartile (i.e., the median of the upper half of the dataset), the horizontal line in the box denotes the median of the dataset, and the whiskers in the figure represent the range of the data. That is, the lower whisker represents the minimum value, and accordingly, the upper whisker represents the maximum value of the dataset [41]. The small number of observed outlier data points are represented by the closed circles.

© 2023 Association for Materials Protection and Performance (AMPP). All rights reserved. No part of this publication may be reproduced, stored in a retrieval system, or transmitted, in any form or by any means (electronic, mechanical, photocopying, recording, or otherwise) without the prior written permission of AMPP.
Positions and opinions advanced in this work are those of the author(s) and not necessarily those of AMPP. Responsibility for the content of the work lies solely with the author(s).

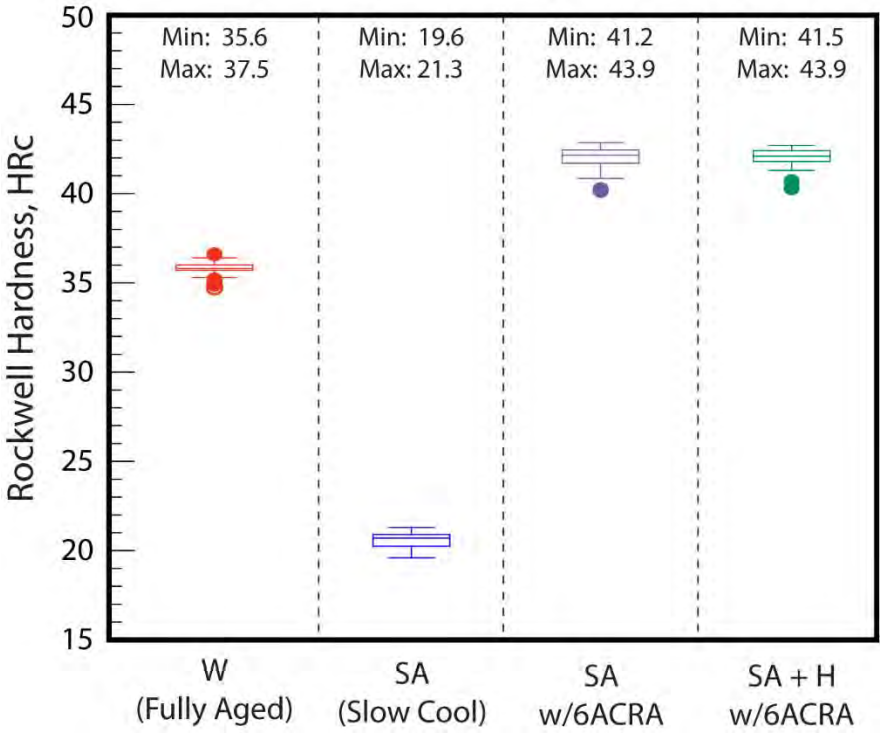

Figure 7: A box and whisker plot showing the relevant statistical parameters derived from the individual HRC test data.

The SA sample was given no aging heat treatment and as expected, the hardness of that sample was considerably lower than the other conditions in the figure. The range of the hardness data from the W sample indicated that the bar was processed using the 6ACRA-120 protocol. The specifications for that condition state that the HRC data must lie between 32 HRC and 40 HRC, and those data clearly are in that range. The most notable result from these analyses was that the hardness values of the SA+6ACRA and the SA+H+6ACRA conditions were statistically identical. This result was somewhat surprising as the initial assumption was that the SA+6ACRA condition would not meet the HRC criteria. However, this was a very important finding for this alloy system. The result indicated that the SA heat treatment protocol (2 h at 1050 °C) solutionized enough of the γ' and γ'' precipitates so that they could sufficiently strengthen the material. Recall that the 6ACRA-150 protocol is a two-stage heat treatment that precipitates both the γ'' and γ' phases. In contrast, the 6ACRA-120 condition is achieved primarily through γ'' precipitation. Further examination of Figure 7 suggested that the γ' precipitate was the component that may have had the stronger influence on the hardness in the 6ACRA-150 condition. This would be consistent with literature accounts showing that γ'' precipitation is more challenging than γ' in this alloy [10, 11]. This could also be one possible explanation for inability to achieve the prescribed HRC values in the 6ACRA-120 condition [12]. Addressing this question requires detailed characterization of the precipitate phases, and those are in progress.

Precipitation in this alloy is a complex process that requires a balance between the formation of the desired phases (γ'' in the 6ACRA-120 condition) against the formation of deleterious phases such as δ-phase and $M_{23}C_6$ carbides. In a wrought material, δ-phase is known to nucleate along grain boundaries, thus promoting intergranular fracture by reducing the grain boundary cohesion. δ-phase has been shown to enhance the sensitivity to hydrogen in wrought IN625, and without proper heat treatment, additive processing exacerbates that sensitivity [21]. Since the performance of an AM component in an environment where hydrogen may be prevalent is a major concern, it is essential to understand the possible co-precipitation of δ-phase and γ'' during aging.

© 2023 Association for Materials Protection and Performance (AMPP). All rights reserved. No part of this publication may be reproduced, stored in a retrieval system, or transmitted, in any form or by any means (electronic, mechanical, photocopying, recording, or otherwise) without the prior written permission of AMPP.
Positions and opinions advanced in this work are those of the author(s) and not necessarily those of AMPP. Responsibility for the content of the work lies solely with the author(s).

The results from a preliminary TC-PRISMA [42] simulation of the precipitation kinetics for the γ'', γ', and the δ-phases are presented in Figure 8. Considering that some of the physical parameters in the IN718 alloy system are similar to those in IN625, the initial simulations were based on the approach used by Lindwall et al [43]. The figure shows the predicted time, temperature, transformation (TTT) behaviors for the three relevant phases. The curves represent the time of the initial formation of the given phase, and in this simulation that corresponded to a phase fraction greater than 0.01. The simulation revealed that δ-phase precipitation begins near 1000°C and reaches a maximum at approximately 950°C, whereas the γ'' phase and γ' phase precipitation occurs at a much lower temperature (≈ 900°C). More importantly, at temperatures below 775°C, the simulation indicates that the kinetics may be somewhat slower for the δ-phase and that precipitation of all three phases will occur at both the γ'' and γ' precipitation temperatures. The initial results indicate that aging below 725°C is more likely to favor the γ'' and γ' precipitation and it may be possible to avoid δ-phase precipitation. Like the phase fractions in Figure 5 and Figure 6, this simulation should be regarded as an estimate. Refinement of the model parameters is in progress.

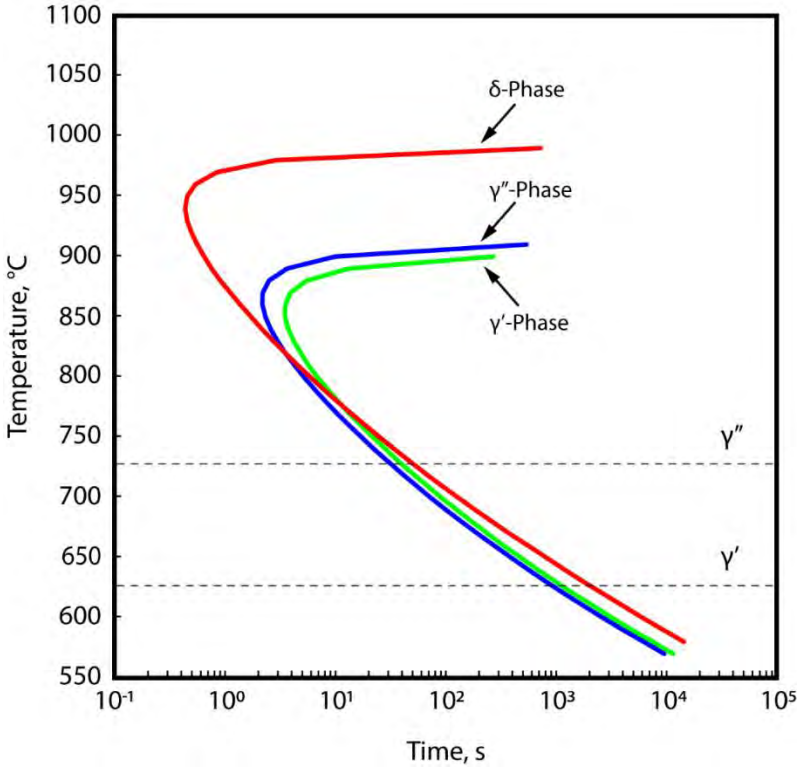

Figure 8: Time, temperature, transformation (TTT) curves for the γ'', γ', and δ-phases predicted by a TC-PRISMA precipitation kinetics simulation.

CONCLUSIONS

Phase-based, multicomponent computational thermodynamic and kinetic tools can be used to optimize the heat-treatment protocol for specific alloy compositions that are within the accepted specification for the alloy composition.

The wrought 6ACRA heat treatment is not sufficient to remove all the AM solidification structure. As such, a higher temperature is recommended; however, the specific temperature and time are dependent on the Nb content in the alloy.

The aging temperature must be optimized based on the Nb content to maximize the γ' and γ'' precipitation and to avoid the precipitation of δ-phase.

© 2023 Association for Materials Protection and Performance (AMPP). All rights reserved. No part of this publication may be reproduced, stored in a retrieval system, or transmitted, in any form or by any means (electronic, mechanical, photocopying, recording, or otherwise) without the prior written permission of AMPP.
Positions and opinions advanced in this work are those of the author(s) and not necessarily those of AMPP. Responsibility for the content of the work lies solely with the author(s).

The Rockwell hardness data revealed that after a 2h at 1050°C solutionizing heat treatment, the γ' precipitation was sufficient to achieve the prescribed hardness for the 6ACRA-150 condition. However, the precipitation of the γ'' phase, which governs the 6ACRA-120 heat treatment, is more difficult to achieve without significant d-phase precipitation.

Rockwell hardness and microstructure characterization were used to establish the initial benchmarks for the alloy in the 6ACRA-150 condition. Additional characterizations are in progress to evaluate the stress-strain behavior and the crack propagation resistance, which is the critical performance metric for this alloy.

ACKNOWLEDGEMENTS

The authors would like to thank Sandra W. Young of the NIST Material Science and Engineering Division for her invaluable assistance with the metallography and the preparation of the samples in this work.

REFERENCES

1. S.S. Babu, L. Love, R. Dehoff, W. Peter, T.R. Watkins, S. Pannala, Additive Manufacturing of Materials: Opportunities and Challenges, MRS Bull., 40,(12), (2015), 1154-1161.
2. W.E. Frazier, Metal Additive Manufacturing: A Review, J. Mater. Eng. Perform., 23,(6), (2014), 1917-1928.
3. G.K. Dey, S. Albert, D. Srivastava, M. Sundararaman, P. Mukhopadhyay, Microstructural Studies on Rapidly Solidified Inconel 625, Mater. Sci. Engr. A, 119, (1989), 175-184.
4. G.P. Dinda, A.K. Dasgupta, J. Mazumder, Laser Aided Direct Metal Deposition of Inconel 625 Superalloy: Microstructural Evolution and Thermal Stability, Mater. Sci. Engr. A, 509,(1–2), (2009), 98-104.
5. M.R. Stoudt, E.A. Lass, D.S. Ng, M.E. Williams, F. Zhang, C.E. Campbell, G. Lindwall, L.E. Levine, The Influence of Annealing Temperature and Time on the Formation of d-Phase in Additively-Manufactured Inconel 625, Metall. Mater. Trans. A, 49,(7), (2018), 3028-3037.
6. F. Zhang, L.E. Levine, A.J. Allen, M.R. Stoudt, G. Lindwall, E.A. Lass, M.E. Williams, Y. Idell, C.E. Campbell, Effect of Heat Treatment on the Microstructural Evolution of a Nickel-Based Superalloy Additive-Manufactured by Laser Powder Bed Fusion, Acta Mater., 152, (2018), 200-214.
7. E.A. Lass, M.R. Stoudt, M.B. Katz, M.E. Williams, Precipitation and Dissolution of d and g″ During Heat Treatment of a Laser Powder-Bed Fusion Produced Ni-Based Superalloy, Scripta Mater., 154, (2018), 83-86.
8. E.A. Lass, M.R. Stoudt, M.E. Williams, M.B. Katz, L.E. Levine, T.Q. Phan, T.H. Gnaeupel-Herold, D.S. Ng, Formation of the Ni_3Nb d-Phase in Stress-Relieved Inconel 625 Produced Via Laser Powder-Bed Fusion Additive Manufacturing, Metall. Mater. Trans. A, 48,(11), (2017), 5547-5558.
9. G. Marchese, M. Lorusso, S. Parizia, E. Bassini, J.-W. Lee, F. Calignano, D. Manfredi, M. Terner, H.-U. Hong, D. Ugues, M. Lombardi, S. Biamino, Influence of Heat Treatments on Microstructure Evolution and Mechanical Properties of Inconel 625 Processed by Laser Powder Bed Fusion, Mater. Sci. & Eng. A, 729, (2018), 64-75.
10. G.H. Cao, T.Y. Sun, C.H. Wang, X. Li, M. Liu, Z.X. Zhang, P.F. Hu, A.M. Russell, R. Schneider, D. Gerthsen, Z.J. Zhou, C.P. Li, G.F. Chen, Investigations of g′, g″ and d Precipitates in Heat-Treated Inconel 718 Alloy Fabricated by Selective Laser Melting, Mater. Char., 136, (2018), 398-406.
11. L. Zhou, A. Mehta, B. McWilliams, K. Cho, Y. Sohn, Microstructure, Precipitates and Mechanical Properties of Powder Bed Fused Inconel 718 before and after Heat Treatment, J. Mater. Sci. Tech., 35,(6), (2019), 1153-1164.

© 2023 Association for Materials Protection and Performance (AMPP). All rights reserved. No part of this publication may be reproduced, stored in a retrieval system, or transmitted, in any form or by any means (electronic, mechanical, photocopying, recording, or otherwise) without the prior written permission of AMPP.
Positions and opinions advanced in this work are those of the author(s) and not necessarily those of AMPP. Responsibility for the content of the work lies solely with the author(s).

12. B. Sutton, E. Herderick, R. Thodla, M. Ahlfors, A. Ramirez, Heat Treatment of Alloy 718 Made by Additive Manufacturing for Oil and Gas Applications, JOM, 71,(3), (2019), 1134-1143.
13. Y. Zhao, K. Li, M. Gargani, W. Xiong, A Comparative Analysis of Inconel 718 Made by Additive Manufacturing and Suction Casting: Microstructure Evolution in Homogenization, Additive Manufacturing, 36, (2020), 101404.
14. W. Huang, J. Yang, H. Yang, G. Jing, Z. Wang, X. Zeng, Heat Treatment of Inconel 718 Produced by Selective Laser Melting: Microstructure and Mechanical Properties, Mater. Sci. & Eng. A, 750, (2019), 98-107.
15. S. Floreen, G.E. Fuchs, W.J. Yang, The Metallurgy of Alloy 625, in: E.A. Loria (Ed.), Superalloys 718, 625, 706 and Various Derivatives, TMS, Warrendale, PA, 1994, pp. 13-37.
16. J. Mittra, S. Banerjee, R. Tewari, G.K. Dey, Fracture Behavior of Alloy 625 with Different Precipitate Microstructures, Mater. Sci. & Eng. A, 574, (2013), 86-93.
17. M. Sundararaman, P. Mukhopadhyay, S. Banerjee, Precipitation of the d-Ni_3Nb Phase in Two Nickel Base Superalloys, Metall. Trans. A, 19,(3), (1988), 453-465.
18. M.J. Benoit, M. Mazur, M.A. Easton, M. Brandt, Effect of Alloy Composition and Laser Powder Bed Fusion Parameters on the Defect Formation and Mechanical Properties of Inconel 625, Int. J. Adv. Manuf. Tech., 114,(3), (2021), 915-927.
19. K. Inaekyan, A. Kreitcberg, S. Turenne, V. Brailovski, Microstructure and Mechanical Properties of Laser Powder Bed-Fused IN625 Alloy, Mater. Sci. Eng. A-Struct. Mater. Prop. Microstruct. Process., 768, (2019), 13.
20. C.U. Brown, G. Jacob, M. Stoudt, S. Moylan, J. Slotwinski, A. Donmez, Interlaboratory Study for Nickel Alloy 625 Made by Laser Powder Bed Fusion to Quantify Mechanical Property Variability, J. Mater. Eng. Perform., 25,(8), (2016), 3390-3397.
21. M. Stoudt, R.E. Ricker, The Influence of Delta-Phase on the Environmentally Assisted Cracking Resistance of an Additively-Manufactured Nickel-Based Superalloy 625, submitted for publication in Metallurgical and Materials Transactions A.
22. Z. Zhang, K.L. Moore, G. McMahon, R. Morana, M. Preuss, On the Role of Precipitates in Hydrogen Trapping and Hydrogen Embrittlement of a Nickel-Based Superalloy, Corro. Sci., 146, (2019), 58-69.
23. W. Xiong, G.B. Olson, Integrated Computational Materials Design for High-Performance Alloys, MRS Bull., 40,(12), (2015), 1035-1044.
24. [24] G.B. Olson, Computational Design of Hierarchically Structured Materials, Science, 277,(5330), (1997), 1237-1242.
25. API Standard 6ACRA: Age-Hardened Nickel-Based Alloys for Oil and Gas Drilling and Production Equipment, American Petroleum Institute, NW Washington DC, 2019.
26. ASTM, ISO/ASTM Designation 52900-15: Standard Terminology for Additive Manufacturing-General Principles- Terminology, ASTM International, West Conshohocken, PA, 2015.
27. NIST Standard Reference Database Number 3: NIST Inorganic Crystal Structure Database, 2022.
28. G.F. VanderVoort, Metallography Principles and Practice, ASM International, Materials Park, OH, 1999.
29. ASTM, ASTM Designation E18-22: Standard Test Methods for Rockwell Hardness of Metallic Materials, ASTM International, West Conshocken, PA, 2022.
30. Thermo-Calc, Thermo-Calc Software AB, Stockholm, Sweden, 2022.
31. TC-Ni11 Ni-Based Alloy Database, Themo-Calc Software AB, Stockholm, Sweden, 2021.

© 2023 Association for Materials Protection and Performance (AMPP). All rights reserved. No part of this publication may be reproduced, stored in a retrieval system, or transmitted, in any form or by any means (electronic, mechanical, photocopying, recording, or otherwise) without the prior written permission of AMPP.
Positions and opinions advanced in this work are those of the author(s) and not necessarily those of AMPP. Responsibility for the content of the work lies solely with the author(s).

32. TC-Mobni5 Ni-Based Alloy Mobility Database, Themo-Calc Software AB, Stockholm, Sweden, 2021.

33. D.A. Porter, K.E. Easterling, Phase Transformations in Metals and Alloys, Chapman and Hall, London, 1981.

34. Scheil Equation, 2022. https://en.wikipedia.org/wiki/Scheil_equation.

35. T. Keller, G. Lindwall, S. Ghosh, L. Ma, B.M. Lane, F. Zhang, U.R. Kattner, E.A. Lass, J.C. Heigel, Y. Idell, M.E. Williams, A.J. Allen, J.E. Guyer, L.E. Levine, Application of Finite Element, Phase-Field, and Calphad-Based Methods to Additive Manufacturing of Ni-Based Superalloys, Acta Mater., 139, (2017), 244-253.

36. Scheil Solidification Simulations, 2022. https://thermocalc.com/products/thermo-calc/scheil-solidification-simulations/.

37. E. Chlebus, K. Gruber, B. Kuźnicka, J. Kurzac, T. Kurzynowski, Effect of Heat Treatment on the Microstructure and Mechanical Properties of Inconel 718 Processed by Selective Laser Melting, Mater. Sci. & Eng. A, 639, (2015), 647-655.

38. A.S. Wilson, Formation and Effect of Topologically Close-Packed Phases in Nickel-Base Superalloys, Mater. Sci. & Tech., 33,(9), (2017), 1108-1118.

39. R.E. Walpole, R.H. Myers, Probability and Statistics for Engineers and Scientists, The Macmillian Co., NY, 1972.

40. W. Mendenhall, T. Sincich, Statistics for Engineering and the Sciences, 3rd ed., Dellen Publishing Co., San Francisco, 1992.

41. Box Plot, 2020. https://en.wikipedia.org/wiki/Box_plot.

42. TC-Prisma, Thermo-Calc Software AB, Stockholm, Sweden, 2022.

43. G. Lindwall, C.E. Campbell, E.A. Lass, F. Zhang, M.R. Stoudt, A.J. Allen, L.E. Levine, Simulation of TTT Curves for Additively Manufactured Inconel 625, Metall. Mater. Trans. A, (2018).

© 2023 Association for Materials Protection and Performance (AMPP). All rights reserved. No part of this publication may be reproduced, stored in a retrieval system, or transmitted, in any form or by any means (electronic, mechanical, photocopying, recording, or otherwise) without the prior written permission of AMPP.
Positions and opinions advanced in this work are those of the author(s) and not necessarily those of AMPP. Responsibility for the content of the work lies solely with the author(s).